論文 / 著書情報
Article / Book Information

Title	Manipulation of the anomalous Hall effect in magnetic topological insulator heterostructure MnBi2Te4/Bi2Te3 by Si substrate surface engineering
Authors	K. Ishihara, S. Ichinokura, S. V. Eremeev, T. T. Sasaki, R. Takada, H. Nishimichi, R. Akiyama, E. V. Chulkov, T. Hirahara
Pub. date	2025, 11
Note	This article may be downloaded for personal use only. Any other use requires prior permission of the author and AIP Publishing. This article appeared in Applied Physics Letters, Volume 127, , and may be found at https://dx.doi.org/10.1063/5.0266580.
Note	This file is author (final) version.

Manipulation of the anomalous Hall effect in magnetic topological insulator heterostructure $MnBi_2Te_4/Bi_2Te_3$ by Si substrate surface engineering

K. Ishihara,[1] S. Ichinokura,[1,a)] S. V. Eremeev,[2] T. T. Sasaki,[3] R. Takada,[1] H. Nishimichi,[1] R. Akiyama,[1] E. V. Chulkov,[4,5,6] and T. Hirahara[1]

[1)]*Department of Physics, Institute of Science Tokyo, Tokyo 152-8551, Japan*
[2)]*Institute of Strength Physics and Materials Science, Tomsk, 634055, Russia*
[3)]*Research Center for Magnetic and Spintronic Materials, National Institute for Materials Science, Tsukuba 305-0047, Japan*
[4)]*Donostia International Physics Center (DIPC), Paseo de Manuel Lardizabal, 4, 20018 San Sebastián/Donostia, Basque Country, Spain*
[5)]*Tomsk State University, Tomsk, 634050, Russia*
[6)]*Saint Petersburg State University, Saint Petersburg, 198504, Russia*

(*Electronic mail: hirahara@phys.sci.isct.ac.jp)

(Dated: 14 September 2025)

We developed an *in situ* Hall measurement setup and measured the anomalous Hall effect (AHE) in magnetic topological insulator heterostructures $MnBi_2Te_4/Bi_2Te_3$ grown on different Si(111) substrate surfaces. For the sample grown on the Si(111)-7×7 surface, the AHE signal appears at 15 K and becomes larger by further cooling, showing that the Curie temperature T_c is 15 K. In contrast, although the T_c is the same, the AHE signal shows a local maximum at 10 K for the sample grown on the β-Bi/Si(111)-$\sqrt{3}\times\sqrt{3}$ surface. A plausible explanation for this peculiar behavior is the enhanced skew scattering caused by the Bi layer, or the presence of the states localized at the interfacial Bi layer, which will affect the Berry curvature of the system. Our results demonstrate the possibility to artificially control the property of a two-dimensional magnet by modification of the substrate surface with a single monatomic layer.

The Hall effect, which is a voltage generated transverse to an electrical current due to the application of a magnetic field or magnetization, is one of the key parameters to discuss quantum properties of materials[1,2]. Among various types of Hall effect, the anomalous Hall effect (AHE) has been regarded as an important physical quantity not only to characterize magnetic systems[3] but also to discuss the Berry curvature in nonmagnets[4].

While experiments to detect the Hall effect have been performed extensively, there are only a few reports that have addressed Hall effect measurements in ultrahigh vacuum (UHV). Even then, the Hall coefficient for non-magnetic systems has only been discussed[5–8], and no AHE measurements have been performed up to now. Due to the rise of various two-dimensional magnets which can be derived from van der Waals layered crystals[9,10] or intrinsic magnetic topological insulators[11,12], the need for a Hall effect measurement system in UHV environment has increased since some systems are not stable in air and capping the surface to prevent oxidation may change the sample magnetization. In this respect, *in situ* characterization is desired to discuss the intrinsic magnetic properties. However, there are hardly any facilities that are capable of performing such experiments. Furthermore, it is desired to simultaneously measure the electronic structure together with macroscopic magnetic properties since the difference in the sample quality as well as the degree of oxidation may also cause confusion in the data interpretation.

Therefore in the present study, we modified our all-in-one multimodal UHV system (Fig. S1) enabling sample fabrication and *in situ* angle-resolved photoemission spectroscopy (ARPES) as well as transport measurements[13,14] and measured the AHE of an intrinsic magnetic topological insulator heterostructure $MnBi_2Te_4/Bi_2Te_3$ (MBT/BT) grown on Si(111) substrates[15] with different surface structures. The Curie temperature was determined as 15 K for all the samples, but we found that the AHE shows a peculiar behavior when the heterostructure was grown on the β-Bi/Si(111)-$\sqrt{3}\times\sqrt{3}$ surface. This likely originates from the skew scattering from the Bi monolayer, or the change in the Berry curvature of the system since the states stemming from this interfacial Bi layer are present near the Fermi level (E_F) and show a crossing with the Dirac cone of MBT/BT. Our results show that a single monatomic layer decoration at the substrate surface can significantly alter the magnetotransport property of a two-dimensional magnet, which is a potentially important point in developing atomic-layer spintronic devices.

The heterostructure samples were prepared by molecular beam epitaxy equipped with a reflection-high-energy electron diffraction (RHEED) system. First, a clean Si(111)-7×7 surface was prepared on an *n*-type substrate (1.5-5 Ωcm resistivity at room temperature) by a cycle of resistive heat treatments. The β-Bi/Si(111)-$\sqrt{3}\times\sqrt{3}$ (hereafter $\beta\sqrt{3}$-Bi) surface was formed by 1 ML (7.83×10^{14} cm^{-2}) of Bi deposition on the 7×7 surface at 620 K monitored by RHEED. Then Bi was deposited either directly on the 7×7 surface or after the formation of the $\beta\sqrt{3}$-Bi surface at ∼250 °C in a Te-rich condition to grow quintuple layer (QL) structured Bi_2Te_3 films and further annealed at ∼250 °C for 5 minutes. This results in a QL by QL growth and the thickness is monitored with

a)Present Address: Center for Basic Research on Materials, National Institute for Materials Science, Tsukuba 305-0003, Japan

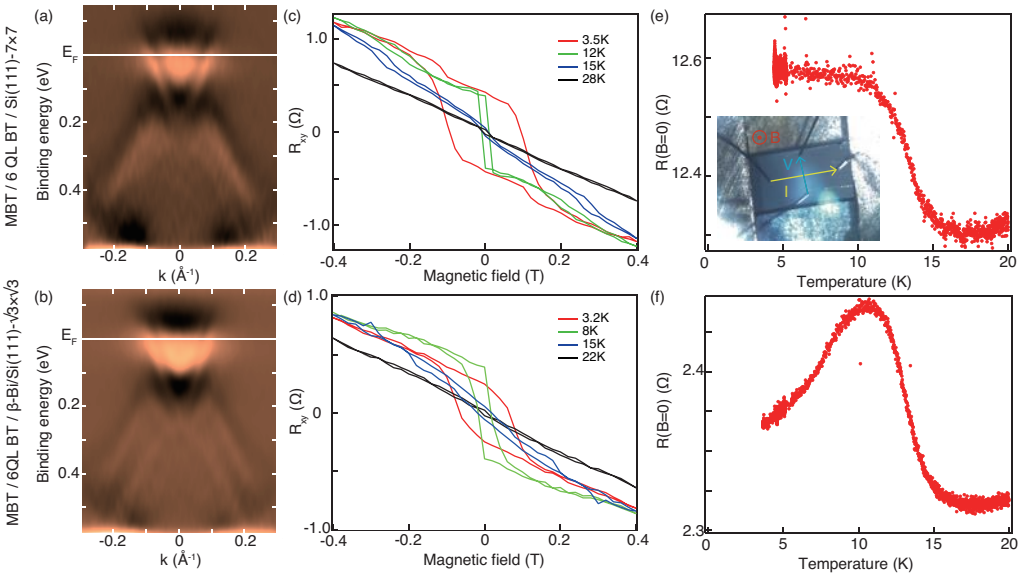

FIG. 1. (a, b) Band dispersion (second derivative) of MBT/ 6 QL BT / Si(111)-7 × 7 (a), and that of MBT / 6 QL BT / β-Bi/Si(111)-$\sqrt{3} \times \sqrt{3}$ (b), respectively, along the $\bar{\Gamma}$-$\bar{M}$ direction measured at room temperature. (c, d) The asymmetrized Hall resistance R_{xy} as a function of the applied magnetic field measured at various temperatures for MBT / 6 QL BT / Si(111)-7 × 7 (c) and MBT / 6 QL BT / β-Bi/Si(111)-$\sqrt{3} \times \sqrt{3}$ (d), respectively. (e, f) Temperature dependence of the measured resistance R at zero field after magnetizing the sample for MBT / 6 QL BT / Si(111)-7 × 7 (e) and MBT / 6 QL BT / β-Bi/Si(111)-$\sqrt{3} \times \sqrt{3}$ (f), respectively. The inset in (e) shows the measurement configuration.

RHEED oscillations. Finally, Mn was deposited on Bi_2Te_3 film in a Te-rich condition at ∼260 °C. The 1 × 1 periodicity with the same lattice constant is maintained during this process for the samples we have fabricated[15,16].

The ARPES measurements were performed after the sample preparation with a commercial hemispherical photoelectron spectrometer equipped with angle and energy multidetections (ScientaOmicron R4000) with He Iα radiation (21.2 eV) at room temperature. Some additional ARPES measurements were performed in a different UHV chamber (ScientaOmicron DA20).

Then, the transport measurements were performed in our custom-made system[13,14] which has four probes that can move independently and by touching the surface of the sample, four-point probe (4PP) resistance measurements can be performed in UHV (Figs. S2, S3). To measure the Hall effect, the probes were aligned in a cross geometry as shown in the inset of Fig. 1(e). The samples were cooled down to ∼3 K in the present study and a magnetic field as large as 0.4 T was applied perpendicular to the sample surface. Although it is not possible to deduce physical parameters quantitatively since we have not fabricated a Hall bar structure, it is still possible to make a qualitative discussion as we will show in the following.

The samples were capped with ∼10 nm of Te before taking them out of the UHV chamber for scanning transmission electron microscopy (STEM) measurements. Electron transparent specimens for STEM observations were prepared by the standard lift-out technique using an FEI Helios G4-UX dual-beam system. Probe abberation corrected STEM, FEI Titan™G2 80-200 microscope, was used. Chemical compositions were measured by energy-dispersive X-ray spectroscopy (EDS).

For structural optimization and electronic band calculations we used the Vienna Ab Initio Simulation Package[17,18] with generalized gradient approximation (GGA-PBE)[19] to the exchange-correlation potential. The interaction between the ion cores and valence electrons was described by the projector augmented-wave method[20,21]. Relativistic effects were taken into account, including the spin-orbit interaction. In order to describe the vdW interactions we made use of the DFT-D3 functional with Becke-Johnson dumping scheme[22]. The geometry optimization was performed until the residual forces on atoms became smaller than 1 meV/Å. To correctly describe the highly correlated Mn-d electrons of MBT we include the correlation effects within the GGA+U method[23] within the Dudarev scheme[24]. The $U_{\text{eff}} = U - J$ value for the Mn 3d-states was chosen to be equal to 5.34 eV[11,25]. For analysis of interactions between atoms at the interfaces we use the projected crystal orbital Hamilton population (pCOHP) method[26,27] implemented within Local-orbital basis suite to-

wards electronic structure reconstruction (LOBSTER) code[28].

Figures 1(a) and (b) show the band dispersion (second derivative) of MBT / 6 QL BT / 7×7 (a), and that of MBT / 6 QL BT / $\beta\sqrt{3}$-Bi (b), respectively, along the $\bar{\Gamma}$-$\bar{\mathrm{M}}$ direction[29]. One can find the linearly dispersion Dirac cone near the Fermi level (E_F) together with the bulk bands, showing that the films are *n*-doped. For the higher binding energy side, there are two bands dispersing away from the $\bar{\Gamma}$ point. These features are basically the same as what is shown in Ref. 15 and demonstrates that two samples apparently do not exhibit significant difference in the surface electronic structure.

However, some difference was observed in the transport data for the two samples. Figures 1(c) and (d) show the Hall resistance R_{xy} as a function of the applied magnetic field measured at various temperatures for MBT / 6 QL BT / 7×7 (c) and MBT / 6 QL BT / $\beta\sqrt{3}$-Bi (d), respectively. These data were asymmerized from the measured raw data R as explained in Fig. S5 to deduce the Hall resistance. It can be noticed that above 20 K, both samples exhibit the normal Hall effect, showing a linear dependence. The negative Hall coefficient shows that the carriers are electrons, consistent with the band dispersion measured with ARPES (Figs. 1(a) and (b)). Upon lowering the temperature, a hysteresis behavior can be observed, demonstrating the detection of the AHE. In Fig. 1(c), the value of R_{xy} at zero field does not change so much for the data at 12 K and 3.5 K, but the value of the magnetic field that R_{xy} crosses zero Ω increases. This shows that the residual magnetization does not increase but the coercive field increases below 12 K. This is a typical behavior of ferromagnets and one can say that the measured AHE is reflecting the magnetization of the MBT/BT heterostructure. Since the contribution of the longitudinal resistance R_{xx} can be expected to be very small in the measured R as shown in Fig. S5, we measured the temperature dependence of $R(B=0)$ after the field sweep to deduce the Curie temperature T_c. As shown in Fig. 1(e), one can find a sharp rise around 15 K by lowering the temperature and this shows that T_c is $\sim$ 15 K. Although we could not detect any signal of ferromagnetism for this sample with *ex situ* XMCD measurements down to 6 K[15], the present measurements unambiguously suggest that the MBT/BT heterostructure grown on Si(111)-7×7 is ferromagnetic below 15 K, which is similar to the report in Ref. 12. The origin of this discrepancy cannot be clearly elucidated at this time.

A qualitatively different behavior was observed for the MBT/BT heterostructure grown on $\beta\sqrt{3}$-Bi. As shown in Fig. 1(d), the clear detection of the hysteresis loop shows that this system is also ferromagnetic. However, although the coercive field is larger for the data at 3.2 K compared to that at 8 K, R_{xy} at zero field is smaller at 3.2 K. This characteristic can be seen more vividly in the temperature dependence of $R(B=0)$ as shown in Fig. 1(f). The signal shows a sharp rise at 15 K, but starts to decrease again below 10 K. This feature is clearly different from the behavior shown in Fig. 1(e) and cannot be explained by a simple effect of typical ferromagnetism.

To elucidate the origin of this peculiar behavior found in AHE, we have performed STEM measurements. Figure 2(a) shows the STEM image for the MBT / 6 QL BT / 7×7. Between the Te capping layer and the Si substrate, the structure can be mostly identified as the designed one. It should be emphasized that at the heterostructure/substrate interface, the image is somehow disturbed. This is due to the fact that disordered Te will build up as a wetting or a buffer layer to saturate dangling bonds of the 7×7 surface[30,31] before the BT growth. In contrast, the heterostructure/substrate interface for the MBT / 6 QL BT / $\beta\sqrt{3}$-Bi shown in Fig. 2(b) has a sharp appearance with a well-defined monolayer. This is likely due to the Bi-trimer layer which originally formed the $\beta\sqrt{3}$-Bi surface reconstruction[32], although we have no evidence whether the in-plane arrangement has changed or not upon the deposition of BT. But the EDS mapping shows that this is a Bi layer as shown in Fig. S6. Since there is hardly any difference in the distribution of unintentionally displaced Mn atoms that can influence the magnetic property as measured by EDS (Fig. S7)[33–37], we conclude that the only clear difference in the atomic structure between the two samples is found at the BT/Si interface.

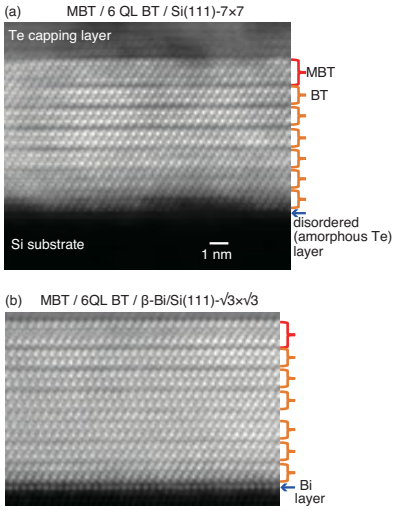

FIG. 2. TEM image of MBT / 6 QL BT / Si(111)-7×7 (a), and that of MBT / 6 QL BT /β-Bi/Si(111)-$\sqrt{3}\times\sqrt{3}$ (b), respectively. The MBT and BT layers are explicitly indicated and the difference in the interface between the Si substrate and the film is emphasized.

It can be anticipated that since the top MBT surface layers which is probed by ARPES is not different for the two systems, the band dispersion shown in Figs. 1(a) and (b) demonstrate no difference. However, because our films are *n*-doped and the bulk carriers are also involved in transport, it can be speculated that the difference in the interface structure can influence the AHE signal. It is known that the band dispersion of BT films grown on Si(111)-7×7 films can be reproduced by DFT calculations for free-standing BT slabs[38]. However, it seems that we need to take into account the Bi layer at the BT/Si interface to describe the electronic structure of BT /

$\beta\sqrt{3}$-Bi. To this end, we have constructed a model shown in Fig. 3(a), in which 5 QL of BT was placed on top of $\beta\sqrt{3}$-Bi. The in-plane lattice constants of BT(111) and Si(111)-$\sqrt{3}\times\sqrt{3}$ differ approximately by factor 1.5 (4.38 vs. 6.69 Å) and hence the better matching between them is realized with superlattices ratio of 3/2, *i.e.* BT(111)-3×3 should be placed on a β-Bi/Si(111) with $2\sqrt{3}\times2\sqrt{3}$ periodicity with 1.9% compression. To simulate the Si(111) substrate we used a slab of two bi-layers (BL) thickness and Hydrogen atoms were used to passivate the Si dangling bonds at the bottom (unreconstructed) surface of the slab. The atomic positions of the bottom BL were fixed at their bulk positions while atoms of the top Si BL as well as β-Bi layer and in the interface QL of BT were relaxed. The calculated band dispersion is depicted in Fig. 3(b) and the different markers show the states localized at different positions in the slab structure.

The bonding energy between Bi-trimer atoms with the underlying Si atoms and that with the nearest Te atoms of the BT were calculated and it turns out that the interaction of BT with the Bi-trimer layer is derived to be about 9 times weaker compared to that between the Bi-trimers and the Si(111) substrate. Due to this weak interaction at the BT/ $\beta\sqrt{3}$-Bi interface, the variation in the interface potential is relatively small and limited to the first (closest to the interface) QL, as shown in Fig. 3(c). This makes the seemingly complicated band dispersion of Fig. 3(b) easy to understand. The states marked by red circles in Fig. 3(b) have their origin as the Rashba-split surface states near the $\bar{\mathrm{K}}$ and $\bar{\mathrm{M}}$ points (Fig. S8(a)) of the$\beta\sqrt{3}$-Bi surface[32], but the energy position has shifted closer to E_{F} due to the change in the potential at the interface. It should also be noted that due to the imposed $2\sqrt{3}\times2\sqrt{3}$ periodicity, the Rashba states of $\beta\sqrt{3}$-Bi are folded to the $\bar{\Gamma}$ point. Similarly, the energy level of the Dirac cone at the top surface (grey circles in Fig. 3(b)) and that at the interface (blue circles) is shifted due to the potential difference at the interface and at the vacuum side of BT.

As discussed above, we are not sure if the above structure model is actually reflecting the situation in the experiment. However, the presence of the bands near the Fermi level localized at the interface Bi layer in addition to the BT Dirac cone seems to be universal irrespective of the presence of the MBT septuple layer at the top (Fig. S8(b)) or whether the BT film thickness is only 1 QL nor the change in stacking between the BT and the β-Bi/Si(111)-$2\sqrt{3}\times2\sqrt{3}$ surface (Figs. S8(c)-(e)). Therefore, we have experimentally tried to confirm the presence of this interface state for the 1 QL BT /$\beta\sqrt{3}$-Bi system. As shown in Fig. S9, there are indeed some features near the Fermi level other than the Dirac cone, but since the intensity is quite weak, we cannot make a direct comparison to the calculated band dispersion. Nevertheless, this shows that interface states localized at the β-Bi interface layer can affect the film property for the MBT / BT grown on the $\beta\sqrt{3}$-Bi surface.

The most simple explanation concerning the unique behavior of the AHE shown in Fig. 1(d) and (f) is that the carriers undergo skew scattering at the interfacial layer and this can give rise to extrinsic AHE due to the strong SOC of Bi. However, since it is well known that the extrinsic mechanism is only dominant for low-mobility (side jump) or high-mobility (skew scattering) systems and most materials can be described by intrinsic effects due to the Berry curvature[2,40], we speculate that the AHE of MBT / 6 QL BT / $\beta\sqrt{3}$-Bi may also be affected by the band structure. One can obviously find that the states originating from the β-Bi layer and the interfacial Dirac cone cross each other (Fig. 3(b)). Such crossing may be a source of Berry curvature, although the actual calculation is beyond the scope of the present work[41]. Nevertheless, we emphasize that the present results demonstrate a convenient way to manipulate the Berry curvature artificially using a single layer at the heterostructure/substrate interface, which can potentially be used to develop spintronic devices using atomically thin magnets.

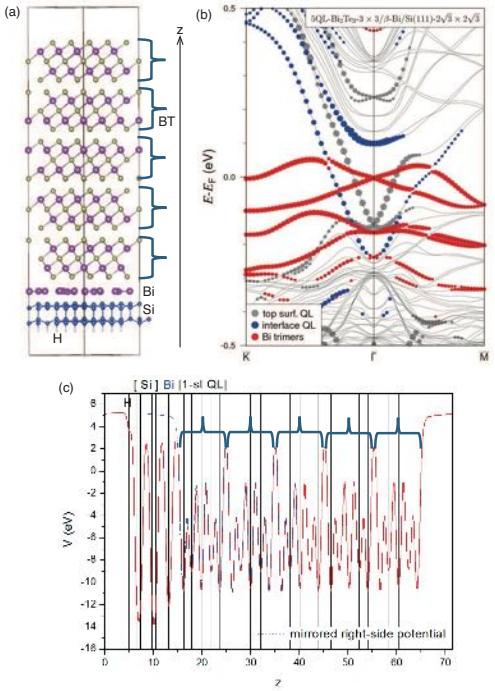

FIG. 3. (a) Atomic structure model (the presented structure was visualized with VESTA[39]) and (b) calculated band dispersion near E_{F} of the 5 QL BT / β-Bi/Si slab. The different markers show the states localized at different positions within the model shown in (a). (c) In-plane (x,y) averaged electrostatic potentials $V(z)$ within the slab. Since the interaction at the Bi/BT interface is weak, there is only a slight change compared to the vacuum/BT interface.

In summary, by means of the developed *in situ* Hall measurement setup, we have shown that the AHE in magnetic topological insulator heterostructures $MnBi_2Te_4/Bi_2Te_3$/Si(111) can be manipulated by controlling the BT/Si interface. The formation of the β-Bi/Si(111)-

$\sqrt{3} \times \sqrt{3}$ surface reconstruction before the heterostructure growth results in appearance a local maximum in the AHE signal at 10 K. This behavior can stem from the skew scattering at the interface, or the effect of the states localized at the Bi interfacial layer that resides at the same energy as the Dirac state of the bottom side of the MBT/BT film, which can affect the Berry curvature of the system.

See supplementary material for details on the instrumental apparatus, linearity of the measured IV curves, raw ARPES data of Figs. 1(a) and (b), data processing in the Hall measurements, EDS mapping of the samples, additional results of DFT calculations, and ARPES data of 1QL BT / $\beta\sqrt{3}$-Bi.

ACKNOWLEDGMENTS

The authors thank M. Uchida, Y. Fuseya, I. A. Shvets, and M. M. Otrokov for stimulating discussions and Y. Fukushima for assisting in the data analyses. T.H. acknowledges the support by Grants-In-Aid from Japan Society for the Promotion of Science (Grants No. 18H03877, No. 22H00293, and No. 23H00268), the Murata Science Foundation (Grant No. H30-084), the Asahi Glass Foundation, the Iketani Science and Technology Foundation (Grant No. 0321083-A), and Support for Tokyo Tech Advanced Researchers. S.V.E. acknowledges support from the Government research assignment for ISPMS SB RAS, project FWRW-2022-0001. E.V.C. acknowledges Saint-Petersburg State University for research Project 116812735.

AUTHOR DECLARATIONS

CONFLICT OF INTEREST

The authors have no conflicts of interest to disclose.

DATA AVAILABILITY

The data that support the findings of this study are available from the corresponding authors upon reasonable request.

[1]E. H. Hall, "On a new action of the magnet on electric currents," American Journal of Mathematics **2**, 287–292 (1879).
[2]N. Nagaosa, J. Sinova, S. Onoda, A. H. MacDonald, and N. P. Ong, "Anomalous Hall effect," Rev. Mod. Phys. **82**, 1539–1592 (2010).
[3]H. Ohno, A. Shen, F. Matsukura, A. Oiwa, A. Endo, S. Katsumoto, and Y. Iye, "(Ga,Mn)As: A new diluted magnetic semiconductor based on GaAs," Applied Physics Letters **69**, 363–365 (1996).
[4]T. Liang, J. Lin, Q. Gibson, S. Kushwaha, M. Liu, W. Wang, H. Xiong, J. A. Sobota, M. Hashimoto, P. S. Kirchmann, Z.-X. Shen, R. J. Cava, and N. P. Ong, "Anomalous Hall effect in $ZrTe_5$," Nature Physics **14**, 451–455 (2018).
[5]I. Vilfan, M. Henzler, O. Pfennigstorf, and H. Pfnür, "Anomalous thickness dependence of the Hall effect in ultrathin Pb layers on Si(111)," Phys. Rev. B **66**, 241306 (2002).
[6]T. Hirahara, I. Matsuda, C. Liu, R. Hobara, S. Yoshimoto, and S. Hasegawa, "Direct measurement of the Hall effect in a free-electron-like surface state," Phys. Rev. B **73**, 235332 (2006).
[7]D. Abdelbarey, J. Koch, Z. Mamiyev, C. Tegenkamp, and H. Pfnür, "Thickness-dependent electronic transport through epitaxial nontrivial Bi quantum films," Phys. Rev. B **102**, 115409 (2020).
[8]J. Koch, S. Sologub, C. Ghosal, T. Tschirner, A. Chatterjee, K. Pierz, H. W. Schumacher, and C. Tegenkamp, "Magnetotransport behavior of epitaxial graphene inhomogeneously doped by Bi(110) islands," Phys. Rev. B **109**, 235107 (2024).
[9]K. S. Burch, D. Mandrus, and J.-G. Park, "Magnetism in two-dimensional van der Waals materials," Nature **563**, 47–52 (2018).
[10]M. Gibertini, M. Koperski, A. F. Morpurgo, and K. S. Novoselov, "Magnetic 2D materials and heterostructures," Nature Nanotechnology **14**, 408–419 (2019).
[11]M. M. Otrokov, I. I. Klimovskikh, H. Bentmann, D. Estyunin, A. Zeugner, Z. S. Aliev, S. Gaß, A. U. B. Wolter, A. V. Koroleva, A. M. Shikin, M. Blanco-Rey, M. Hoffmann, I. P. Rusinov, A. Y. Vyazovskaya, S. V. Eremeev, Y. M. Koroteev, V. M. Kuznetsov, F. Freyse, J. Sánchez-Barriga, I. R. Amiraslanov, M. B. Babanly, N. T. Mamedov, N. A. Abdullayev, V. N. Zverev, A. Alfonsov, V. Kataev, B. Büchner, E. F. Schwier, S. Kumar, A. Kimura, L. Petaccia, G. Di Santo, R. C. Vidal, S. Schatz, K. Kißner, M. Ünzelmann, C. H. Min, S. Moser, T. R. F. Peixoto, F. Reinert, A. Ernst, P. M. Echenique, A. Isaeva, and E. V. Chulkov, "Prediction and observation of an antiferromagnetic topological insulator," Nature **576**, 416–422 (2019).
[12]P. Kagerer, C. I. Fornari, S. Buchberger, T. Tschirner, L. Veyrat, M. Kamp, A. V. Tcakaev, V. Zabolotnyy, S. L. Morelhão, B. Geldiyev, S. Müller, A. Fedorov, E. Rienks, P. Gargiani, M. Valvidares, L. C. Folkers, A. Isaeva, B. Büchner, V. Hinkov, R. Claessen, H. Bentmann, and F. Reinert, "Two-dimensional ferromagnetic extension of a topological insulator," Phys. Rev. Res. **5**, L022019 (2023).
[13]A. K. Pedersen, S. Ichinokura, T. Tanaka, R. Shimizu, T. Hitosugi, and T. Hirahara, "Interfacial superconductivity in FeSe ultrathin films on $SrTiO_3$ probed by in situ independently driven four-point-probe measurements," Phys. Rev. Lett. **124**, 227002 (2020).
[14]K. Ide, T. Tanaka, A. Pedersen, S. Ichinokura, and T. Hirahara, "Temperature dependence of the superconducting gap of single-layer $FeSe/SrTiO_3$: Direct comparison between transport and spectroscopic measurements," Phys. Rev. Mater. **6**, 124801 (2022).
[15]T. Fukasawa, S. Kusaka, K. Sumida, M. Hashizume, S. Ichinokura, Y. Takeda, S. Ideta, K. Tanaka, R. Shimizu, T. Hitosugi, and T. Hirahara, "Absence of ferromagnetism in $MnBi_2Te_4/Bi_2Te_3$ down to 6 K," Phys. Rev. B **103**, 205405 (2021).
[16]T. Hirahara, M. M. Otrokov, T. T. Sasaki, K. Sumida, Y. Tomohiro, S. Kusaka, Y. Okuyama, S. Ichinokura, M. Kobayashi, Y. Takeda, K. Amemiya, T. Shirasawa, S. Ideta, K. Miyamoto, K. Tanaka, S. Kuroda, T. Okuda, K. Hono, S. V. Eremeev, and E. V. Chulkov, "Fabrication of a novel magnetic topological heterostructure and temperature evolution of its massive Dirac cone," Nature Communications **11**, 4821 (2020).
[17]G. Kresse and J. Hafner, "Ab initio molecular dynamics for open-shell transition metals," Phys. Rev. B **48**, 13115–13118 (1993).
[18]G. Kresse and J. Furthmüller, "Efficient iterative schemes for ab initio total-energy calculations using a plane-wave basis set," Phys. Rev. B **54**, 11169–11186 (1996).
[19]J. P. Perdew, K. Burke, and M. Ernzerhof, "Generalized gradient approximation made simple," Phys. Rev. Lett. **77**, 3865–3868 (1996).
[20]P. E. Blöchl, "Projector augmented-wave method," Phys. Rev. B **50**, 17953–17979 (1994).
[21]G. Kresse and D. Joubert, "From ultrasoft pseudopotentials to the projector augmented-wave method," Phys. Rev. B **59**, 1758–1775 (1999).
[22]S. Grimme, S. Ehrlich, and L. Goerigk, "Effect of the damping function in dispersion corrected density functional theory," Journal of Computational Chemistry **32**, 1456–1465 (2011).
[23]V. I. Anisimov, J. Zaanen, and O. K. Andersen, "Band theory and Mott insulators: Hubbard U instead of Stoner I," Phys. Rev. B **44**, 943–954 (1991).
[24]S. L. Dudarev, G. A. Botton, S. Y. Savrasov, C. J. Humphreys, and A. P. Sutton, "Electron-energy-loss spectra and the structural stability of nickel oxide: An LSDA+U study," Phys. Rev. B **57**, 1505–1509 (1998).
[25]S. V. Eremeev, M. M. Otrokov, and E. V. Chulkov, "Competing rhombohedral and monoclinic crystal structures in $MnPn_2Ch_4$ compounds: An ab-initio study," Journal of Alloys and Compounds **709**, 172–178 (2017).

[26]R. Dronskowski and P. E. Bloechl, "Crystal orbital Hamilton populations (COHP): energy-resolved visualization of chemical bonding in solids based on density-functional calculations," The Journal of Physical Chemistry **97**, 8617–8624 (1993).
[27]V. L. Deringer, A. L. Tchougréeff, and R. Dronskowski, "Crystal orbital Hamilton population (COHP) analysis as projected from plane-wave basis sets," The Journal of Physical Chemistry A **115**, 5461–5466 (2011).
[28]S. Maintz, V. L. Deringer, A. L. Tchougréeff, and R. Dronskowski, "LOBSTER: A tool to extract chemical bonding from plane-wave based DFT," Journal of Computational Chemistry **37**, 1030–1035 (2016).
[29]The raw data can be found in Fig. S4.
[30]T. Shirasawa, J. Tsunoda, T. Hirahara, and T. Takahashi, "Structure of a Bi/Bi_2Te_3 heteroepitaxial film studied by x-ray crystal truncation rod scattering," Phys. Rev. B **87**, 075449 (2013).
[31]Y. Liu, G. Bian, T. Miller, M. Bissen, and T.-C. Chiang, "Topological limit of ultrathin quasi-free-standing Bi_2Te_3 films grown on Si(111)," Phys. Rev. B **85**, 195442 (2012).
[32]K. Sakamoto, H. Kakuta, K. Sugawara, K. Miyamoto, A. Kimura, T. Kuzumaki, N. Ueno, E. Annese, J. Fujii, A. Kodama, T. Shishidou, H. Namatame, M. Taniguchi, T. Sato, T. Takahashi, and T. Oguchi, "Peculiar Rashba splitting originating from the two-dimensional symmetry of the surface," Phys. Rev. Lett. **103**, 156801 (2009).
[33]Y. Liu, L.-L. Wang, Q. Zheng, Z. Huang, X. Wang, M. Chi, Y. Wu, B. C. Chakoumakos, M. A. McGuire, B. C. Sales, W. Wu, and J. Yan, "Site mixing for engineering magnetic topological insulators," Phys. Rev. X **11**, 021033 (2021).
[34]Y. Lai, L. Ke, J. Yan, R. D. McDonald, and R. J. McQueeney, "Defect-driven ferrimagnetism and hidden magnetization in $MnBi_2Te_4$," Phys. Rev. B **103**, 184429 (2021).
[35]S. X. M. Riberolles, Q. Zhang, E. Gordon, N. P. Butch, L. Ke, J.-Q. Yan, and R. J. McQueeney, "Evolution of magnetic interactions in Sb-substituted $MnBi_2Te_4$," Phys. Rev. B **104**, 064401 (2021).
[36]M. Sahoo, I. J. Onuorah, L. C. Folkers, E. Kochetkova, E. V. Chulkov, M. M. Otrokov, Z. S. Aliev, I. R. Amiraslanov, A. U. B. Wolter, B. Büchner, L. T. Corredor, C. Wang, Z. Salman, A. Isaeva, R. De Renzi, and G. Allodi, "Ubiquitous order-disorder transition in the Mn antisite sublattice of the $(MnBi_2Te_4)(Bi_2Te_3)_n$ magnetic topological insulators," Advanced Science **11**, 2402753 (2024).
[37]R. Fukushima, V. N. Antonov, M. M. Otrokov, T. T. Sasaki, R. Akiyama, K. Sumida, K. Ishihara, S. Ichinokura, K. Tanaka, Y. Takeda, D. P. Salinas, S. V. Eremeev, E. V. Chulkov, A. Ernst, and T. Hirahara, "Direct evidence of induced magnetic moment in Se and the role of misplaced Mn in $MnBi_2Se_4$-based intrinsic magnetic topological insulator heterostructures," Phys. Rev. Mater. **8**, 084202 (2024).
[38]Y.-Y. Li, G. Wang, X.-G. Zhu, M.-H. Liu, C. Ye, X. Chen, Y.-Y. Wang, K. He, L.-L. Wang, X.-C. Ma, H.-J. Zhang, X. Dai, Z. Fang, X.-C. Xie, Y. Liu, X.-L. Qi, J.-F. Jia, S.-C. Zhang, and Q.-K. Xue, "Intrinsic topological insulator Bi_2Te_3 thin films on Si and their thickness limit," Advanced Materials **22**, 4002–4007 (2010).
[39]K. Momma and F. Izumi, "*VESTA 3* for three-dimensional visualization of crystal, volumetric and morphology data," Journal of Applied Crystallography **44**, 1272–1276 (2011).
[40]T. Miyasato, N. Abe, T. Fujii, A. Asamitsu, S. Onoda, Y. Onose, N. Nagaosa, and Y. Tokura, "Crossover behavior of the anomalous Hall effect and anomalous Nernst effect in itinerant ferromagnets," Phys. Rev. Lett. **99**, 086602 (2007).
[41]To perform such calculations it is necessary to construct the localized Wannier function basis from the Bloch function basis derived from the DFT calculations. However, for the BT/β-Bi/Si(111) interface model which contains huge number of atoms and which spectrum is very complex, the construction of large number of Wannier functions, accurately describing the spectrum, is highly problematic. On the other hand, the Berry's curvature is very sensitive to the spectrum accuracy. Moreover, one needs to consider the temperature effect to understand why the AHE shows a maximum at 10 K.

Supplementary material for "Manipulation of the anomalous Hall effect in magnetic topological insulator heterostructure $MnBi_2Te_4/Bi_2Te_3$ by Si substrate surface engineering"

K. Ishihara,[1] S. Ichinokura,[1,*] S. V. Eremeev,[2] T. T. Sasaki,[3] R. Takada,[1] H. Nishimichi,[1] R. Akiyama,[1] E. V. Chulkov,[4,5,6] and T. Hirahara[1,†]

[1] *Department of Physics, Institute of Science Tokyo, Tokyo 152-8551, Japan*
[2] *Institute of Strength Physics and Materials Science, Tomsk, 634055, Russia*
[3] *Research Center for Magnetic and Spintronic Materials, National Institute for Materials Science, Tsukuba 305-0047, Japan*
[4] *Donostia International Physics Center (DIPC), Paseo de Manuel Lardizabal, 4, 20018 San Sebastián/Donostia, Basque Country, Spain*
[5] *Tomsk State University, Tomsk, 634050, Russia*
[6] *Saint Petersburg State University, Saint Petersburg, 198504, Russia*

I. INSTRUMENTAL

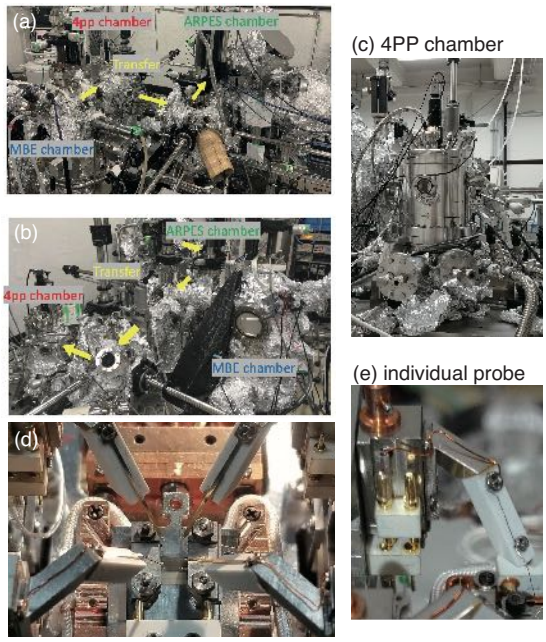

FIG. S1. (a, b) Sequence of the experiment. After the sample is fabricated in the MBE chamber, it is transferred to the ARPES chamber for *in situ* electronic structure characterization. Then it is transferred to the 4PP chamber for *in situ* transport measurements. (c) The picture of the 4PP chamber taken from the back side. (d) The picture of 4 probes together with the sample. (e) A close-up picture of an individual probe.

Figure S1 shows the instrument used in the present measurements. A silicon wafer (3 mm×10 mm×0.5 mm) is mounted on an Omicron-type sample holder fixed with two electrodes made of Ta that enables direct current heating. The heterostructure samples were fabricated in the MBE chamber, and transferred to the ARPES chamber for *in situ* electronic structure characterization (Fig. S1(a)). Then it was transferred to the 4PP chamber for *in situ* transport measurements (Fig. S1(b)). The measurement can be performed in the reverse order if needed.

Figure S1(c) shows the picture of the 4PP chamber taken from the back side. It has two tanks and the outer tank is filled with liquid nitrogen and the inner one with liquid helium. With proper pumping, the sample temperature can

* Present Address: Center for Basic Research on Materials, National Institute for Materials Science, Tsukuba 305-0003, Japan
† hirahara@phys.sci.isct.ac.jp

reach ∼3 K. Inside the chamber, 4 probes are placed at the sample stage, as shown in Fig. S1(d). The probe position is monitored with a CCD camera from the top. The probes currently used are made of Cu wires with a diameter of 0.1 mm as shown in the enlarged picture of Fig. S1(e).

The 4 probes can move independently in xyz directions with piezo-drivers by applying high voltage. After adjusting the in-plane x and y positions of the 4 probes, the probes approach the sample by moving in the z direction. Whether the tip has approached the sample surface can be confirmed not only from the CCD camera image, but also by checking the resistance between the probe and sample (the electrodes that fix the sample as shown in Fig. S1(d)). When all four of the probes make contact with the sample, the resistance between various pairs of probes (2 Probe resistance) is checked, as shown in Fig. S2. After confirming that they are normal, 4PP measurements can be conducted.

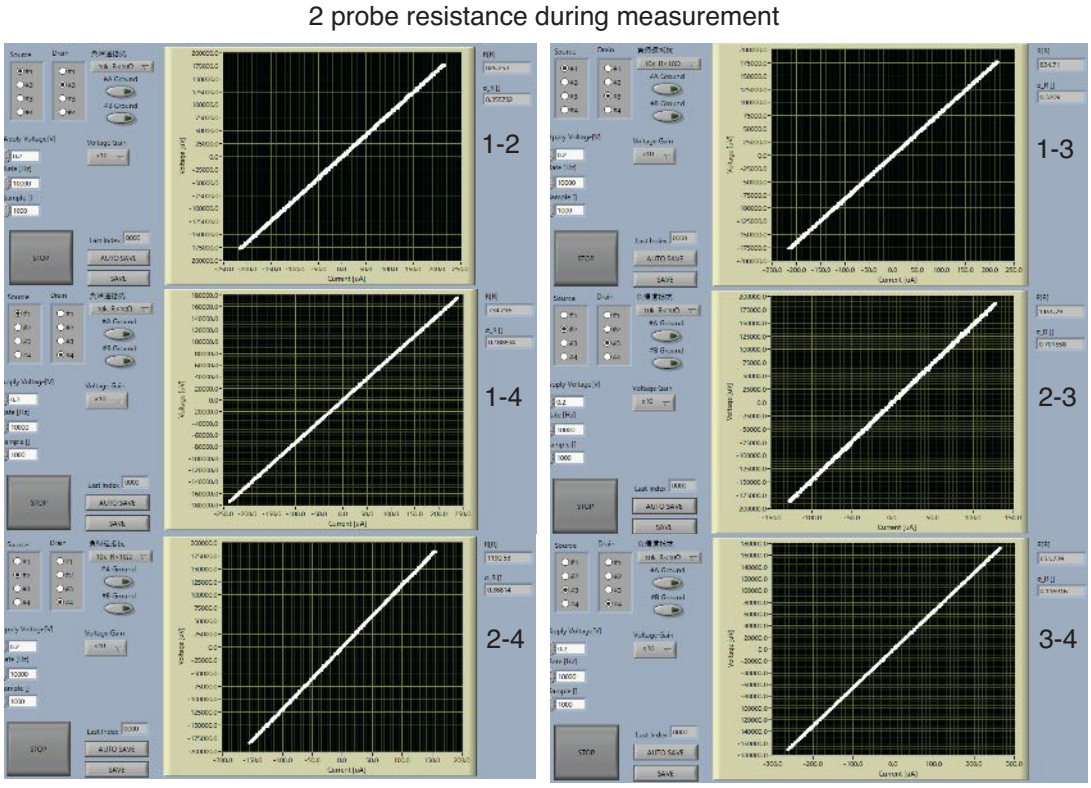

FIG. S2. Contact resistance (2 probe resistance) between various pair of probes during the measurement.

A home-made superconducting coil with a μ-metal magnetic core inside is placed just under the sample stage, and a magnetic field as large as 0.6 T can be applied perpendicular to the sample surface as calibrated by putting a Hall sensor when the sample holder was not placed in the sample stage. Figure S3 shows the magnetic field dependence of the measured resistance measured simultaneously for the two different configurations of current and voltage probes. All the measured 4 probe resistance is deduced from linear IV curves, and the measured results of the two different configurations show nearly the same tendency qualitatively. As mentioned in the main text, since it is impossible to deduce quantitatively correct values in our measurements, we discuss the results shown by the red configuration in the main text.

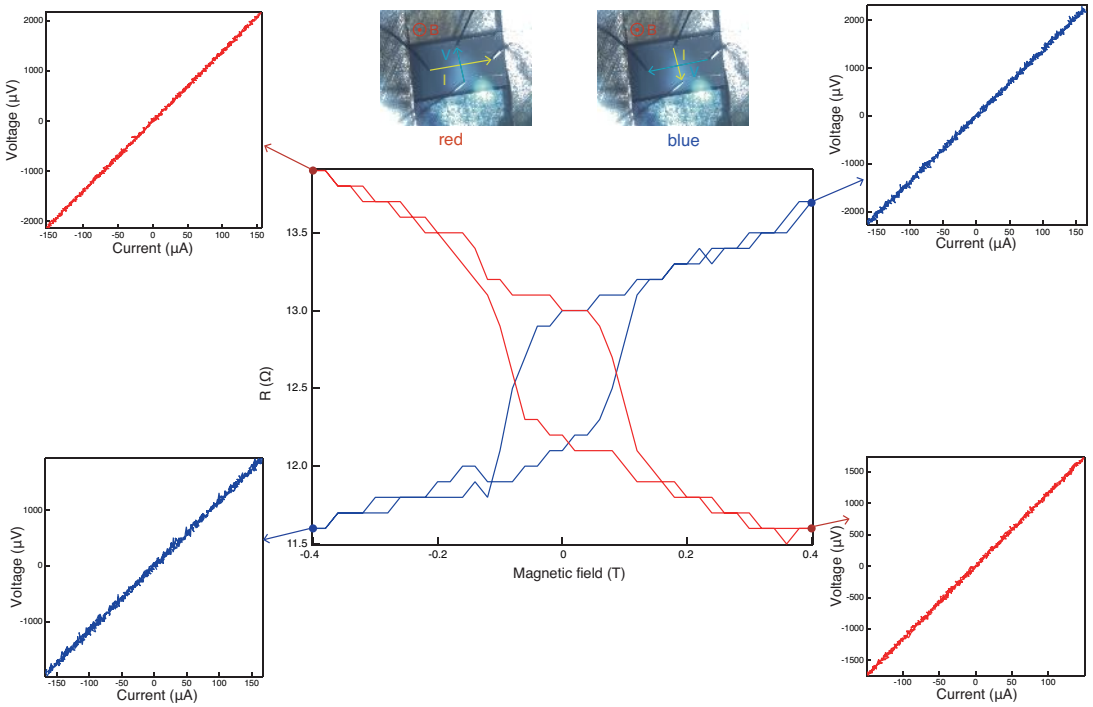

FIG. S3. Actual IV curves during the measurement as well as the magnetic field dependence of the measured resistance for different probe configurations.

II. RAW ARPES DATA

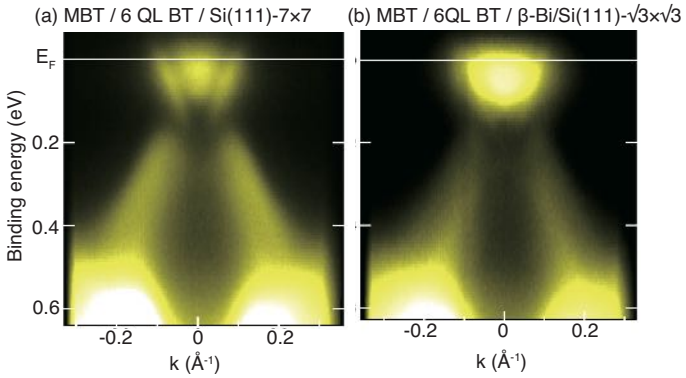

FIG. S4. Raw ARPES data of the MBT / 6 QL BT / Si(111)-7 × 7 (a) and MBT / 6 QL BT / β-Bi/Si(111)-$\sqrt{3} \times \sqrt{3}$ (b), respectively.

Figures S4(a) and (b) show the raw data of the band dispersion of the MBT / 6 QL BT / Si(111)-7 × 7 (a) and MBT / 6 QL BT / β-Bi/Si(111)-$\sqrt{3} \times \sqrt{3}$ (b), respectively.

III. EXTRACTION OF THE HALL RESISTANCE R_{xy} AND THE LONGITUDINAL RESISTANCE R_{xx} FROM THE RAW DATA

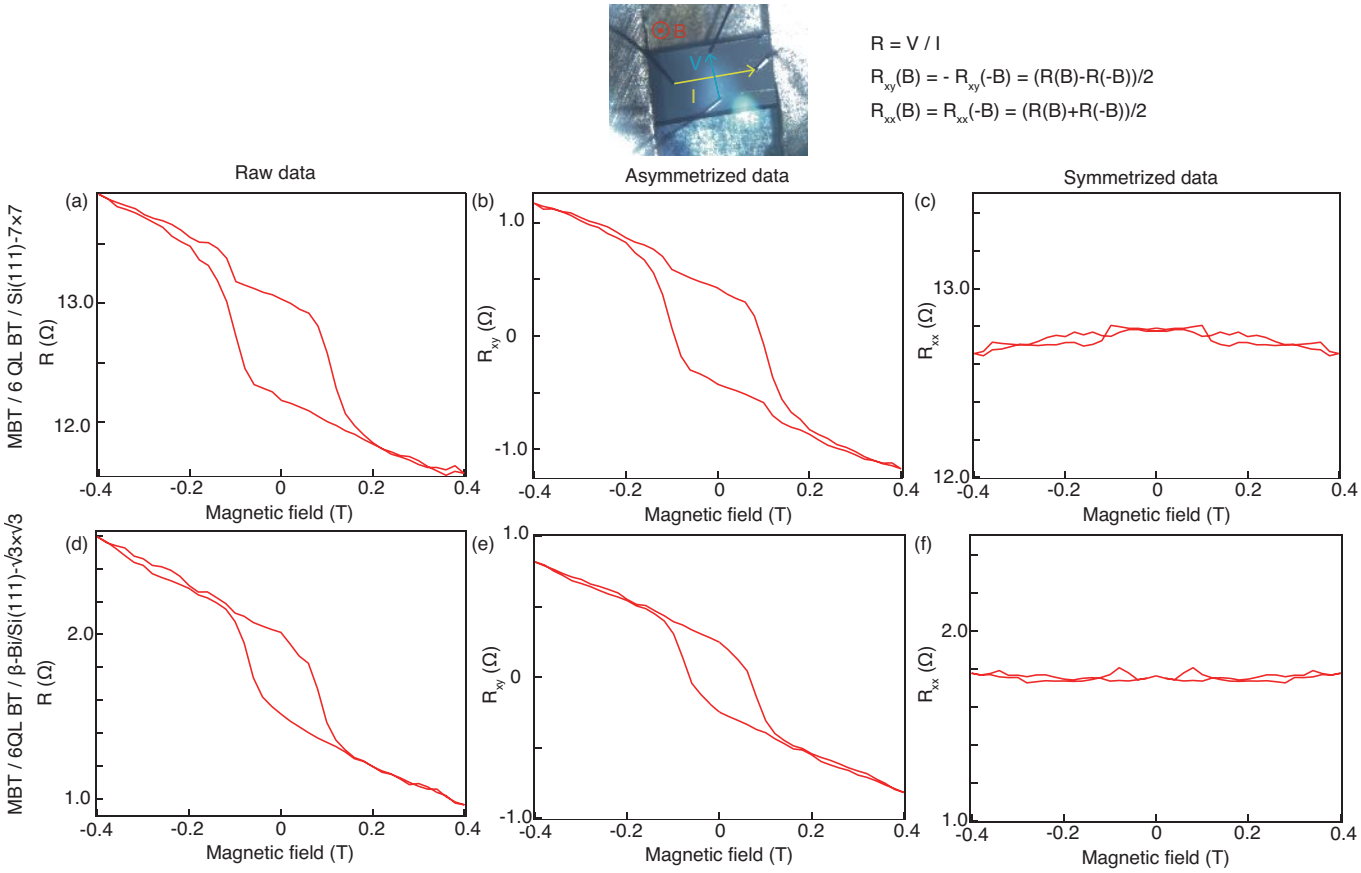

FIG. S5. (a, b, c) Raw data at ∼3 K deduced by V/I (a), the Hall resistance R_{xy} derived by asymmetrizing the raw data (b), and the longitudinal resistance R_{xx} derived by symmetrizing the raw data (c), respectively, for MBT / 6 QL BT / Si(111)-7×7. (d, e, f) Same as (a), (b), and (c) but for MBT / 6 QL BT / β-Bi/Si(111)-$\sqrt{3}\times\sqrt{3}$. The top panel shows the measurement configuration as well as the equations for asymmetrization and symmetrization.

Figures S5(a) and (d) show the raw data $R = V/I$ for the MBT / 6 QL BT / Si(111)-7×7 (a) and MBT / 6 QL BT / β-Bi/Si(111)-$\sqrt{3}\times\sqrt{3}$ (d), respectively, measured at ∼3 K. One can notice that there is slight asymmetry between the data points at positive and negative magnetic field due to the misalignment of the voltage probes. Therefore, the Hall resistance R_{xy} is derived by asymmetrizing the raw data [(b) and (e)], and the longitudinal resistance R_{xx} is deduced by symmetrizing the raw data [(c) and (f)].

IV. EDS MAPPING AT THE Si/BT INTERFACE FOR MBT / 6 QL BT / $\beta - \mathrm{Bi/Si(111)} - \sqrt{3} \times \sqrt{3}$

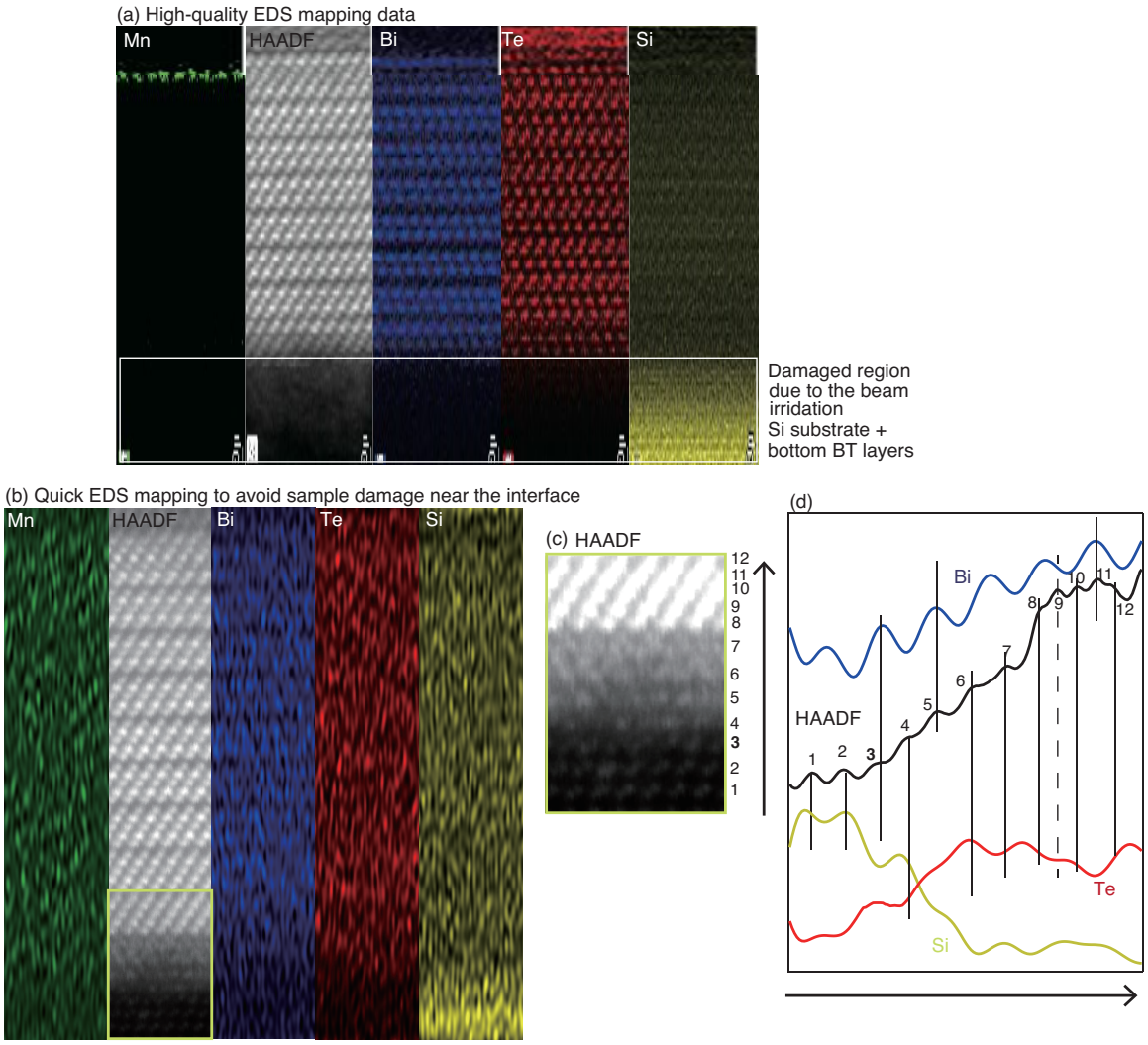

FIG. S6. (a) Close-up of the MBT layers in the TEM images. (b) Comparison of the EDS mapping of Mn at the MBT layers for MBT / 6 QL BT / Si(111)7×7 (red) and MBT / 6 QL BT / β-Bi/Si(111)-$\sqrt{3} \times \sqrt{3}$ (blue).

EDS mapping is a powerful tool to identify each element in STEM images. Figure S6 (a) shows the element specific as well as HAADF image of the MBT / 6 QL BT / β-Bi/Si(111)-$\sqrt{3} \times \sqrt{3}$ sample. It can clearly be seen that we have fabricated the desired structure, but near the interface to the Si substrate one can notice that sample has been damaged and each atom cannot be resolved clearly. This sometimes happens because to get high-quality data in EDS, the electron beam is irradiated to the sample for a very long time. For the present samples, the bottom BT QL as well as the Si substrate is the most damaged region and to identify the elements near the BT/Si interface is quite challenging. Nevertheless, we have obtained evidence that the interfacial layer between Si and BT is composed of Bi. Figure S6 (b) shows similar data as Fig. S6 (a) measured quickly and it is evident that the each element is not well distinguished in the images. However, by taking a line profile of each atoms in the film thickness direction, it is possible to resolve the elements of each layer. Figure S6 (c) shows the contrast-enhanced magnified HAADF image near the BT/Si interface and Fig. S6 (d) shows the element resolved line profile of each element together with that of the clear HAADF image. From these data, it is evident that there is a Bi layer (labeled 3) at the interface between Si and BT.

In conclusion, since the interface region of the sample is easily damaged by the high-energy electron beam, it is difficult to perform this kind of EDS mapping measurement, but it can be said that the additional monolayer at the interface is composed of Bi.

V. DISTRIBUTION OF MISPLACED Mn ATOMS

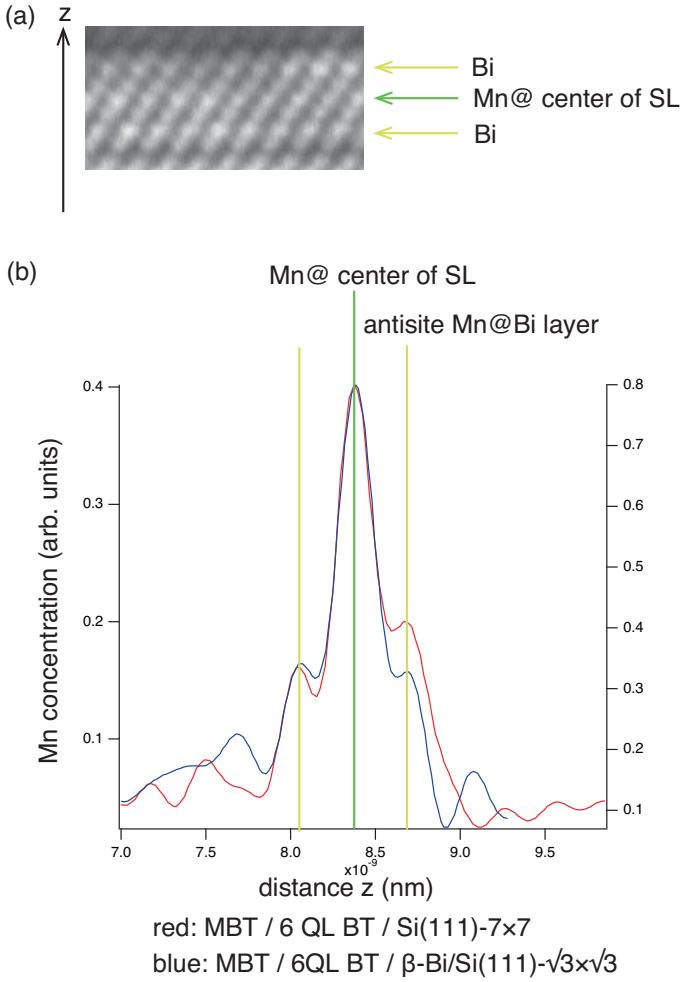

FIG. S7. (a) Close-up of the MBT layers in the TEM images. (b) Comparison of the EDS mapping of Mn at the MBT layers for MBT / 6 QL BT / Si(111)7×7 (red) and MBT / 6 QL BT / β-Bi/Si(111)-$\sqrt{3} \times \sqrt{3}$ (blue).

Since it is known that the misplaced Mn atoms at the Bi layers (antisite Mn) couple antiferromagnetically to the Mn at the center of the SL in MBT[1–4], one can anticipate that the magnetic property of the system can change depending on the degree of the misplacement of the Mn atoms. To verify this effect, we have performed a detailed analyses using EDS for the present samples. Figure S7 (a) shows the close-up of the MBT layers in the STEM images. The septuple layer (SL) structure is clear visible. Figure S7 (b) shows the comparison of the the EDS mapping of Mn at the MBT layers for MBT / 6 QL BT / Si(111)7×7 (red) and MBT / 6 QL BT / β-Bi/Si(111)-$\sqrt{3} \times \sqrt{3}$ (blue). It can be noticed that the distribution of these antisite Mn is not so different, meaning that the effect of misplaced Mn on the magnetic property is the same for both samples.

VI. CALCULATED BAND DISPERSION FOR DIFFERENT SLAB GEOMETRIES

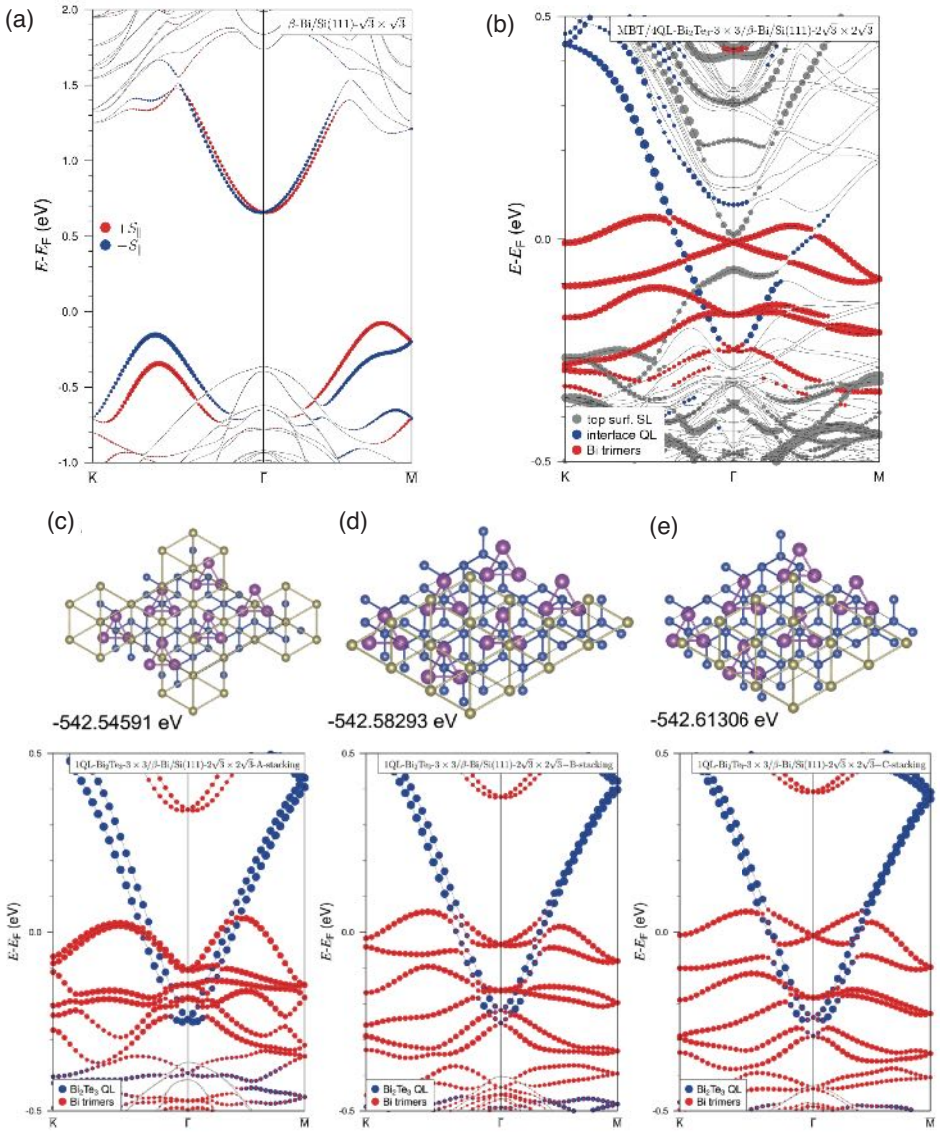

FIG. S8. (a) Calculated band dispersion of the β-Bi/Si(111)-$\sqrt{3} \times \sqrt{3}$ surface. (a) Calculated band dispersion of the MBT / 4 QL BT / β-Bi/Si(111)-$\sqrt{3} \times \sqrt{3}$ slab. (c, d, e) Calculated band dispersion of the 1 QL BT / β-Bi/Si(111)-$\sqrt{3} \times \sqrt{3}$ slab for different stacking. The calculated total energy for each stacking is also shown.

Figure S8 (a) shows the calculated band dispersion of the β-Bi/Si(111)-$\sqrt{3} \times \sqrt{3}$ surface. The Rashba-split surface states can be recognized [5]. Figure S8 (b) shows the calculated band dispersion of the MBT / 4 QL BT / β-Bi/Si(111)-$\sqrt{3} \times \sqrt{3}$ slab. Although the Dirac cone at the top surface becomes gapped due to the out-of-plane spin polarization of Mn, the dispersion of the interfacial Bi layer states do not change compared to that shown in Fig. 4(b). Figures S8 (c)-(e) show the calculated band dispersion of the 1 QL BT / β-Bi/Si(111)-$\sqrt{3} \times \sqrt{3}$ slab for different stacking. In fact, there can be an arbitrary in-plane shift between the substrate and the BT adlayer, but the cases considered contain a variety of local configurations between bottom Te atoms and Bi trimers (like Te ontop Bi, Te above the center of the trimer, Te in different positions in-between Bi trimers), so we can limit ourselves to these structures. Again, the dispersion of the interfacial Bi layer states do not change significantly compared to that shown in Fig. 4(b).

VII. EXPERIMENTAL VERIFICATION OF THE ELECTRONIC STATES FROM THE INTERFACE Bi LAYER

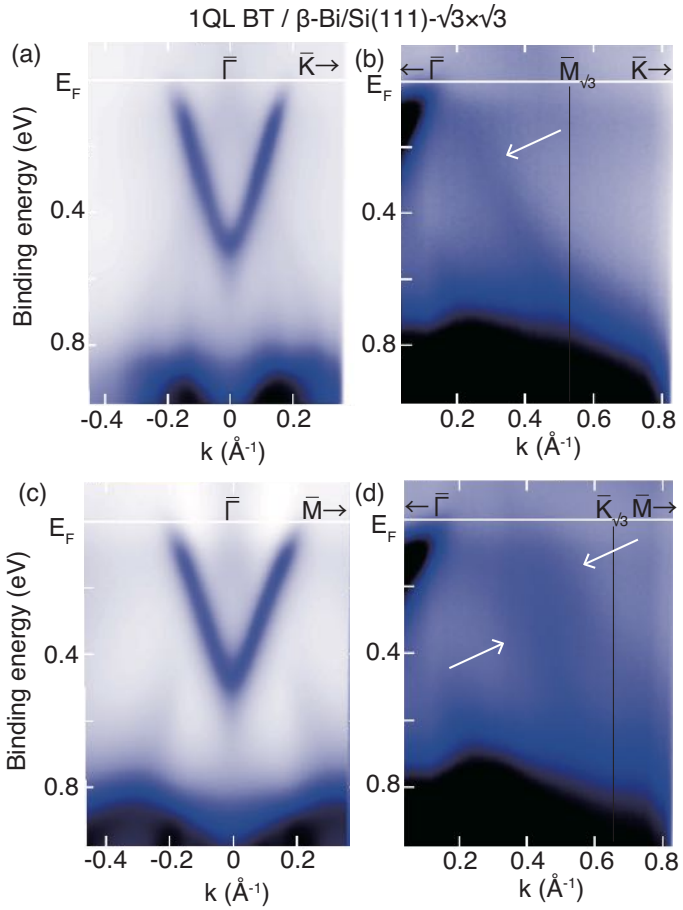

FIG. S9. (a, b) Band dispersion of the 1 QL BT / β-Bi/Si(111)-$\sqrt{3} \times \sqrt{3}$ sample along the $\bar{\Gamma}$-$\bar{\mathrm{K}}$ direction, which corresponds to the $\bar{\Gamma}$-$\bar{\mathrm{M}}$ direction in the $\sqrt{3} \times \sqrt{3}$ Brillouin zone. (c, d) Band dispersion of the 1 QL BT / β-Bi/Si(111)-$\sqrt{3} \times \sqrt{3}$ sample along the $\bar{\Gamma}$-$\bar{\mathrm{M}}$ direction, which corresponds to the $\bar{\Gamma}$-$\bar{\mathrm{K}}$ direction in the $\sqrt{3} \times \sqrt{3}$ Brillouin zone.

Figure S9 show the experimentally measured band dispersion of the 1 QL BT / β-Bi/Si(111)-$\sqrt{3} \times \sqrt{3}$ sample at the $\bar{\Gamma}$ point [(a) and (c)] as well as those near the $\bar{\mathrm{M}}_{\sqrt{3}}$ (b) and $\bar{\mathrm{K}}_{\sqrt{3}}$ (d) points, respectively. Although the features are very weak compared to the clearly observed Dirac cone, one can notice that there are some states near the Fermi level indicated by the arrows and although a direct comparison to the calculation shown in Fig. 4(b) as well as Fig. S3 is difficult, they likely originate from the β-Bi layer at the Si/BT interface.

[1] Y. Liu, L.-L. Wang, Q. Zheng, Z. Huang, X. Wang, M. Chi, Y.Wu, B. C. Chakoumakos, M. A. McGuire, B. C. Sales, W. Wu,and J. Yan, Phys. Rev. X **11**, 021033 (2021).

[2] Y. Lai, L. Ke, J. Yan, R. D. McDonald, and R. J. McQueeney, Phys. Rev. B **103**, 184429 (2021).

[3] S. X. M. Riberolles, Q. Zhang, Elijah Gordon, N. P. Butch,Liqin Ke, J.-Q. Yan, and R. J. McQueeney, Phys. Rev. B **104**,064401 (2021).

[4] M. Sahoo, I. Onuorah, L. Folkers, E. Chulkov, M. Otrokov,Z. Aliev, I. Amiraslanov, B. Büchner, L. Corredor, C. Wang,Z. Salman, A. Isaeva, R. De Renzi, and G. Allodi, Adv. Sci.e2402753 (2024).

[5] K. Sakamoto, H. Kakuta, K. Sugawara, K. Miyamoto, A. Kimura, T. Kuzumaki, N. Ueno, E. Annese, J. Fujii, A. Kodama, T. Shishidou, H. Namatame, M. Taniguchi, T. Sato, T. Takahashi, and T. Oguchi, Phys. Rev. Lett. **103**, 156801 (2009).